Physics of the Earth and Planetary Interiors 306 (2020) 106505

Contents lists available at ScienceDirect

Physics of the Earth and Planetary Interiors

journal homepage: www.elsevier.com/locate/pepi

Ferric iron in bridgmanite and implications for ULVZs

Joshua M.R. Muir[a,b,*], John P. Brodholt[b]

[a] Institute of Geochemistry, Chinese Academy of Sciences, 99 West Lincheng Road, Guiyang, Guizhou 550081, China
[b] Department of Earth Sciences, University College London, Gower Street, London WC1E 6BT, UK

ARTICLE INFO

Keywords:
Bridgmanite
Ultra-low velocity zones
Ferric iron
DFT

ABSTRACT

The seismic velocities of ferric iron-enriched bridgmanite under core-mantle boundary (CMB) conditions were calculated using GGA + U ab initio molecular dynamics to probe whether ferric iron enriched mantle can explain the properties of ultra-low velocity zones (ULVZ). Under these conditions ferric iron demonstrated some unusual properties.

The effect of ferric iron on the 0 K transition pressure of the bridgmanite (bdg) to postperovskite (ppv) transition with GGA + U has some dependence upon the value of U_{eff} that is set for B site ferric iron which is in contrast to most substances where U_{eff} has little effect on the properties. We find that ferric iron can both stabilise and destabilise the bdg phase relative to the ppv phase depending upon the value of U_{eff}. This is due to the spin state transition of B-site ferric iron and was not seen in ferrous or aluminous ferric bridgmanite which lack such a transition at mantle conditions. Due to the similar energies and pressure derivatives of the bdg and ppv phases very subtle energy changes (such as that of iron clustering or different theoretical or experimental setups) can have large effects on the relative phase stabilities at different pressures.

The spin state of ferric iron in bdg demonstrates some novel behaviours. With large iron enrichment the spin state of the B site has a non-linear dependence on concentration and depends upon the local arrangement of iron. At typical lower mantle pressures, ferric iron is expected to be high spin in the A site and low spin at the B site but at the temperatures of the CMB thermal spreading of the electrons causes ferric iron at the B site to become high spin.

This is not a typical "spin transition" however as it involves no structural rearrangement of the unit cell and is predicted to have no effect on the elasticity and thus the seismicity of the crystal.

Our elasticity results show that at the CMB ferric iron-enriched bridgmanite has nearly identical V_p and V_s to ferrous iron-bearing bridgmanite, and thus bridgmanite containing large amounts of Fe^{2+} or Fe^{3+} can both explain ULVZ properties when mixed with ferropericlase. We find, however, that mixing of both ferric and ferrous iron in bridgmanite causes a large (up to 1 km/s) non-ideal decrease in V_p when there is middling amounts of ferric iron. This non-linear mixing should have significant effects throughout the lower mantle whenever such amounts of ferric iron are present though such a ferrous:ferric ratio would typically require an increase of the natural ferrous:ferric ratio (for example through very high oxidation fugacities or chemical doping). In the case of ULVZs this non-linear mixing significantly impairs the fitting to some ULVZ data sets (those with a $d\ln V_s/d\ln V_p \sim 3$), but greatly improves the fitting to other ULVZ data sets (those with a $d\ln V_s/d\ln V_p \sim 1$).

The oxidation state of highly enriched iron in bridgmanite at CMB conditions has, therefore, a large effect on the ability of mantle mixtures that are highly enriched in iron to replicate ULVZ properties.

1. Introduction

One of the most puzzling features of the lowermost mantle are seismic observations of ultra-low velocity zones (ULVZ). These are small regions in the lowermost mantle generally < 100 km wide and about 5–40 km thick characterised by large density (5–15%) and velocity contrasts (−5–15% in V_p and −20–45% in V_s) compared to the surrounding mantle (see for example Thorne et al. (2013), Jensen et al. (2013), McNamara et al. (2010), Cottaar and Romanowicz (2012). There are currently two main hypotheses for their origin; one is that they are small regions of partial melt, and the other is that they are regions of strongly iron-enriched mantle. Their high-density means that

* Corresponding author at: Institute of Geochemistry, Chinese Academy of Sciences, 99 West Lincheng Road, Guiyang, Guizhou 550081, China.
E-mail address: j.m.r.muir@mail.gyig.ac.cn (J.M.R. Muir).

https://doi.org/10.1016/j.pepi.2020.106505
Received 1 April 2018; Received in revised form 16 April 2020; Accepted 12 May 2020
Available online 15 May 2020
0031-9201/

a partial melt, if it exists, must also be Fe-enriched. Both hypotheses have positives and negatives. Firstly, it difficult to maintain mounds of dense partial melt over long periods of time without the melt draining out or the ULVZ spreading out (Hernlund and Jellinek, 2010) which is a problem if ULVZs are regarded as a persistent feature over geologic time. On the other hand, the variation in V_s is generally much larger than the variation in V_p ($dlnV_s/dlnV_p \sim 3$) which is more suggestive of melt than of a compositional variation in a solid. However, not all ULVZs are the same and a recent study on a ULVZ beneath the Coral Sea (Brown et al., 2015) found that both V_p and V_s decreased by about 25% each, giving $dlnV_s/dlnV_p \sim 1$. They suggested that this ULVZ has a compositional origin rather than a partial melt. Rather than different compositional origins this large variety in ULVZ properties may also be reflective of large tradeoffs in seismological measurements- for example thickness and velocity values are intertwined (Bower et al., 2011) as are ULVZ morphology and distribution (Zhao et al., 2017). These problems increase the need to know the underlying mineral physics parameter spaces.

Recent work has shown that highly ferrous iron enriched ferropericlase (fp) (Wicks et al., 2010; Bower et al., 2011; Muir and Brodholt, 2015a; Wicks et al., 2017) in combination with less enriched bridgmanite (bdg) (or vice versa) can explain some ULVZ properties. Studies of the effect of ferric iron on the properties of bdg under lower mantle conditions and whether this has an effect on ULVZ properties are largely inconclusive and need more examination. In this work, therefore, we theoretically examine the elasticity of ferric-iron enriched bridgmanite with a focus on the high pressure and high temperature conditions of the CMB (136 GPa 2000–4000 K).

While the effect of ferrous iron on bridgmanite elasticities is straightforward (e.g. Dorfman and Duffy (2014) and Shukla et al. (2015b)), the effect of ferric iron on the elasticities of bridgmanite is more complex. Some studies have found that ferric iron increases the bulk modulus (K) (Andrault et al., 2001; Dorfman and Duffy, 2014; Nishiyama et al., 2007; Nishio-Hamane et al., 2008), while others have found the opposite and that K decreases with ferric iron concentration (Ballaran et al., 2012; Li et al., 2005; Saikia et al., 2009; Liu et al., 2018). Some of this discrepancy can be explained due to differences in both how ferric iron is present and how the spin transition is treated. In Aluminous bridgmanite ferric iron typically occupies the A site and Al the B site whereas in Al-free bridgmanite ferric iron occupies both the A and the B site (Shukla et al., 2016; Shukla and Wentzcovitch, 2016; Glazyrin et al., 2014; Catalli et al., 2011; Sinmyo, 2017; Kupenko et al., 2014; Kurnosov et al., 2017). This is important because iron in these different sites have different spin properties and thus different elastic properties.

Ferric iron at the A site is typically high spin throughout lower mantle pressures whereas B site ferric iron has a transition from high to low spin at ~40–70 GPa which strongly affects elasticities (Shukla et al., 2016; Shukla and Wentzcovitch, 2016; Glazyrin et al., 2014; Catalli et al., 2011; Sinmyo, 2017; Fujino et al., 2014; Kurnosov et al., 2017; Kupenko et al., 2014; Zhang et al., 2016; Wang et al., 2015; Mao et al., 2015; Hsu et al., 2011) and thus the pressure range and the background chemistry of experiments has a very large effect on the elastic results.

By using ab initio methods these two effects can be controlled for. With these methods Shukla et al. (2016), Zhang et al. (2016) and Wang et al. (2015) have suggested that the seismic velocities of ferric iron bearing bridgmanite is similar to ferrous iron containing bridgmanite when aluminium is present, and around 3–5% slower (with an additional spin state discontinuity) when aluminium is not present. These theoretical studies, however, do not explore the high temperatures of the CMB and only explore low concentrations of Fe^{3+} which is reasonable for most of the mantle but is not suitable for the highly enriched phases required to explain ULVZs. Additionally, the coexistence of ferric and ferrous iron may have non-linear effects on the elasticity as has been seen experimentally with an iron-rich bridgmanite (Ismailova et al., 2016) and this has not been explored theoretically.

In this paper, therefore, we examine the properties of bridgmanite at much higher concentrations of ferric iron than has previously been studied theoretically (all the way up to Fe_2O_3) under CMB conditions, and we examine the co-effect of ferrous- and ferric- iron on the elasticity of bridgmanite.

A final consideration comes from the phase structure of ferric-enriched bridgmanite at conditions of the CMB. While bridgmanite with a perovskite structure (bdg) is stable through most of the lower mantle at the D" it possibly undergoes a transition to post-perovskite (ppv) and then back to bdg with depth as increasing pressure favours the ppv phase and increasing temperature favours the bdg phase (Murakami et al., 2005; Hernlund et al., 2005). There has been considerable debate on the exact position of this transition as it is heavily dependent upon the background chemistry in which it occurs (Grocholski et al., 2012) with both Fe and Al having large effects on this transition. Ferrous iron has been seen to lower the onset pressure of ppv formation and broaden the transition (Sun et al., 2018; Caracas and Cohen, 2005; Dorfman and Duffy, 2014; Mao et al., 2004) but in the presence of ferropericlase it can raise this pressure (and sharpen the transition) due to partitioning effects (Catalli et al., 2009; Grocholski et al., 2012). Fe−Al pairs deepen the transition while also greatly broadening it (Grocholski et al., 2012; Sun et al., 2018; Akber-Knutson et al., 2005; Nishio-Hamane et al., 2007; Andrault et al., 2010; Catalli et al., 2009; Tateno et al., 2005). These effects, however, are again heavily dependent on the other phases that are present- which affects partitioning- and it is likely in pyrolitic compositions that there is no simple seismic signature and phase transition and that local heterogeneity will lead to both bridgmanite and post-perovskite being stable at a range of depths across the lowermost mantle including the CMB (Grocholski et al., 2012; Sun et al., 2018).

The case of pure ferric iron in bridgmanite is more complicated. Pure Fe_2O_3 has multiple stable phases at high pressures which complicates the $MgSiO_3$-Fe_2O_3 phase diagram. Rh_2O_3 phases are stable at high pressures but at CMB pressures and temperatures pure Fe_2O_3 should exist in the ppv phase alongside mixed valence phases (Bykova et al., 2016). This Fe_2O_3 ppv phase forms at lower pressures (60–73 GPa) than the ppv phase in $MgSiO_3$ (~100 GPa) which would generally suggests that ferric iron stabilises the ppv phase in bridgmanite but the significant differences between $MgSiO_3$ and Fe_2O_3 end members means that this generalisation might not hold for lower concentrations of ferric iron.

Shukla et al. (2015a) calculated with DFT that in contrast to ferrous iron which destabilises the bdg phase in favour of the ppv phase ferric iron has a strong stabilisation effect of the bdg phase. With iron contents of $x = 0.125$ they found that the bdg to ppv phase transition pressure was increased by 10 GPa when this iron was ferric but it decreased by around 10 GPa when this iron was ferrous. As the transition of perovskite to post perovskite occurs at roughly ~125 GPa at deep lower mantle temperatures a stabilisation of the perovskite phase of this order would make the perovskite phase stable at the CMB for large amounts of ferric iron. Further evidence for a stabilisation of the bdg phase by ferric iron comes from partitioning studies. Studies of the partitioning of iron between bridgmanite and ferropericlase phases shows that the ratio of ferric to ferrous iron drops considerably on conversion of bridgmanite to the ppv phase which suggests that ferric iron prefers- and thus stabilises- the bdg phase (Gialampouki et al., 2018; Piet et al., 2016). Calculations by Wang et al., 2019 show that both ferric and ferrous iron increase ppv stability (lower the transition depth) in both static and high temperature conditions whereas aluminous ferric iron increases bdg stability at static conditions but decreases it at high temperatures. It was also found in this work that all 3 of these additions sufficiently broadens the two-phase region where both bdg and ppv are present. This two phase region is likely to be significant near both the D" and CMB with large amounts of iron. In this study we primarily examine the effects of ferric iron on the elasticity of the bdg

phase but we shall also examine the stability of the bdg phase compared to ppv phase in the presence of ferric iron.

2. Methods

2.1. Theoretical setup

All simulations were carried out with VASP (Kresse and Furthmuller, 1996) using the projector-augmented-wave (PAW) method (Kresse and Joubert, 1999) and the PBE formulation of GGA (Perdew et al., 1996; Perdew et al., 1997). For Mg atoms the semicore 2p states were treated as valence and for Fe atoms the semicore 3p states were treated as valence. Traditional DFT does not deal well with heavily correlated electrons such as the d electrons of transition metals and so some kind of correction is needed to accurately capture electron energy levels. For this we used the Hubbard U approach (where an additional localised energy penalty is introduced for intra-atomic interactions) and we used the rotationally invariant formulation of LSDA + U introduced by Dudarev et al. (1998). A value of U_{eff} (U-J) needs to be set. Hsu et al. determined self-consistent values of U_{eff} of 2.9 eV for ferrous iron (Hsu et al., 2010) 3.7 for high spin A site ferric iron and 3.2 for high spin B site ferric iron (Hsu et al., 2011). As we are dealing with the variation of spin at temperature and with both ferric and ferrous iron we, following Huang and Pan 2012, applied a flat U_{eff} of 3.0 to all Fe 3d orbitals. The value of U_{eff} does not typically vary the properties of the system as long as it correctly predicts the spin state of the Fe in the unit cell(Muir and Brodholt, 2015b) and so this value of U_{eff} should be sufficient for predicting elasticities of the different spin states of ferric bearing bridgmanite. A flat U_{eff} becomes problematic only when calculating the transition of bdg to the ppv phase (as discussed in that section) and so when calculating this transition 3 different methods were used: a flat value of U set to 3 eV and 4.5 eV and self-consistent values taken from Shukla et al. (2015a) of bdg: Fe^{2+} 3.1, Fe^{3+} A Site 3.7, B site HS 3.3, B Site LS 4.9 ppv: Fe^{2+} 2.9, Fe^{3+} A Site 4.0, B site HS 3.5, B Site LS 5.6.

Static runs were calculated with (4x4x2) k-points and molecular dynamics runs were calculated at the gamma point. To ensure k point sufficiency we tested larger k point meshes for both unstrained and strained unit cells and found no difference in output stresses or in atom vibrations for dynamic runs. Static calculations had an energy cutoff of 850 eV and were converged to within 10^{-6} eV. For the molecular dynamics simulations we used a cutoff of 550 eV and electronic energies were converged to 10^{-4} eV. Molecular dynamics (MD) trajectories were propagated in the *NVT* ensemble with the Nosé thermostat (Nose, 1984) for 6–10 ps (10 ps for undeformed states, 6 ps for strained states). For high temperature molecular dynamics simulations the full kinetic contribution was included in the calculation of the stress tensor (Hess and Evans, 2001). Nosé frequencies were ~20 THz. In MD runs all irons were paramagnetic.

2.2. Systems examined

Free energy and elasticity simulations on ferric-iron bearing bridgmanite ($Fe_{2x}Mg_{1-x}Si_{1-x}O_3$) were performed at pressures of 30, 80 and 136 GPa and at temperatures of 0, 2000 K and 4000 K and with Fe contents of x = 0.125, 0.25, 0.5 and x = 1. For ferrous/ferric containing bridgmanite ($Fe_{x+\ y}Mg_{1-x}Si_{1-y}O_3$) elasticity simulations were run at 80 and 136 GPa at 0, 2000 and 4000 K and with compositions of $Fe_{0.5}Mg_{0.5}SiO_3$, $Fe_{0.5}Mg_{0.5625}Si_{0.9375}O_3$, $Fe_{0.5}Mg_{0.625}Si_{0.875}O_3$, $Fe_{0.5}Mg_{0.6875}Si_{0.8125}O_3$ and $Fe_{0.5}Mg_{0.75}Si_{0.75}O_3$. For transitions between the bridgmanite and post-perovskite crystal structures we used $Fe_{2x}Mg_{1-x}Si_{1-x}O_3$, $Fe_xMg_xSiO_3$ and $Fe_xMg_{1-x}Al_xSi_{1-x}O_3$ with various x values (as listed in the tables) and static calculations at 4 pressure points with 5 GPa between them spread around the transition pressure. It was assumed that vibrational entropy effects will be minimal in calculating the effect of iron or aluminium on the perovskite/post-perovskite phase change.

Unless otherwise stated all iron in the systems were arranged in their most enthalpically stable position which sees the A-site iron at maximum separation along (110) rows. B site iron is then positioned at the next nearest neighbour to the iron occupied A site.

All runs were performed with an 80 atom unit cell (2a*2b*c) – simulations performed on a 160 unit cell structure produced the same cell sizes and relative energies in both static and dynamic tests.

2.3. Spin states and elasticity runs

Three types of calculations were performed: ones where the total spin was fixed so that both A and B sites were in the high-spin state (HS-HS), ones where the spin was fixed to a low-spin state (LS-LS) and a third set of calculations where the spin was allowed to find its own value. In all lower mantle conditions it was found that these calculations led to a HS at the A site and a low spin at the B site (HS-LS) regardless of starting condition and thus these calculations provide free energy for HS-LS cases. There is never a case where B is high spin and A is low spin (Sinmyo (2017) among others) and so this can be ignored. The proportion of high spin and low spin iron was determined using Eq. (1):

$$n_{LS}(P,T) = \frac{1}{1 + \exp\left(\frac{\Delta G_{LS-HS}}{n_{Fe} KT}\right)} \quad (1)$$

where n_{LS} is the proportion of states in a particular site (A or B) in the low spin state, ΔG is the free energy change (including magnetic, vibrational and electronic entropy) going from the high-spin to low-spin state for either the A or B site, n_{Fe} is the number of iron atoms per unit cell (Wentzcovitch et al., 2009) and K is the Boltzmann constant. The determination of ΔG uses a thermodynamic integration and is discussed in the supplementary method.

Isothermal elastic constants were calculated by applying four strain magnitudes (± 0.02 and ± 0.01) to three axial and one triclinic strain. The calculation of adiabatic elastic constants is the same as in Muir and Brodholt (2015b). To determine the elasticity of states with a mixed spin state we used a simple weighting method from Wu and Wentzcovitch (2014) which we outline in the supplementary methods. Statistical uncertainties in MD runs were determined via the blocking method (Flyvbjerg and Petersen, 1989) and then propagated to elastic constants and entropies via weighted least squares fitting methods.

3. Results

3.1. The presence of post perovskite phases

As explained in the introduction it is unclear what phase ferric-enriched bridgmanite should be in at the CMB. To examine this we calculated the pressure of the bdg to ppv conversion at 0 K (static DFT) for $Fe_{2x}Mg_{1-x}Si_{1-x}O3$ and $Fe_xMg_{1-x}SiO_3$ and $Fe_xMg_{1-x}Al_xSi_{1-x}O_3$ (Table 1). With this we assume that the primary effect of iron on the phase transition is enthalpic with thermal changes being minimal- calculations of the thermal effect by Wang et al. (2019) find that ferrous and ferric iron do not have large effects on the Clapeyron slope of the transition though they do significantly broaden the transition with temperature.

We find that the pressure of the $MgSiO_3$ bdg to ppv transition (94.2/98.0 GPa for LDA/GGA respectively) is lowered significantly with ferrous iron (x = 0.25 72.3/79.3) and raised for Aluminous ferric iron (x = 0.25103.9/108.8).

With pure ferric iron, however, we find that the case is more complex as we find the ferric iron both stabilises and destabilises the pv phase depending upon the value of Hubbard U_{eff} that we set. With a flat value of U_{eff} (3 eV) applied to all iron atoms we find that ferric iron stabilises the ppv phase (x = 0.25 65.9/71.8) but by using the self-

Table 1
Static GGA transition pressure (in GPa) for the bdg to ppv phase transition for ferrous, ferric and alumino-ferric bridgmanite containing various amounts of Fe. U values were either set to equal for all iron or set to different amounts based on Shukla et al. (2015a).

$MgSiO_3$ = 97.95 GPa				
	x			
	0.0625	0.125	0.25	0.5
$Fe_xMg_{1-x}SiO_3$				
U_{eff} = 4.5		90.2	81.5	
U_{eff} = 3	93.3	88.6	79.3	70.0
Varied	93.0	88.0	75.5	63.1
$Fe_{2x}Mg_{1-x}Si_{1-x}O_3$				
U_{eff} = 4.5		82.6	78.7	
U_{eff} = 3	86.3	76.7	71.8	42.2
Varied	120.0	137.6	150.0	110.6
$Fe_xMg_{1-x}Al_xSi_{1-x}O_3$				
U_{eff} = 3	101.6	105.2	108.8	112.4
Varied	101.1	104.2	107.3	110.4

consistent U_{eff} values of Shukla et al. (2015a) we find that ferric iron instead stabilises the bdg phase (x = 0.25145.2/150 GPa) as was also found by Shukla et al 2015. To confirm our U_{eff} value wasn't too low we also ran selected points with U_{eff} = 4.5 eV where ferric iron still stabilised the ppv phase (x = 0.25 84.1/78.5 GPa). Typically U_{eff} values have negligible effects on the properties if the spin states are correctly predicted (Muir and Brodholt, 2015b) but in this case a dramatic variation in transition pressure is seen with different U_{eff} values. The reason that this dramatic reliance on U_{eff} is seen (and is not seen for ferrous iron or aluminous ferric iron) is due to ferric iron on the B site. This atom has a spin transition that is close in pressure to the phase transition (which is not the case for ferrous or ferric iron on the A site) and bdg and ppv have very similar dE/dP values. Thus slight changes in the energies of relative spin states (as occurs with variations in U_{eff}) and their dE/dP values lead to large changes in phase transition pressures- this is particularly the case with self-consistent U_{eff} as the different spin states have different U_{eff} values and thus different energies. This perhaps explains why a different study in the literature that also used self-consistent U_{eff} values and LDA pseudopotentials found that ferric iron stabilises the ppv phase (Wang et al., 2019) in contrast to the work of Shukla et al. 2015. Slight differences in the U_{eff} values between these two studies could lead to very large differences in spin transition pressure even if the other computational parameters are fairly similar.

We clarify here that the proximity of the spin state transition pressure in B site ferric iron to the phase transition pressures causes the dependence of ferric iron transitions on U_{eff} rather than any stabilisation of the bdg phase. The introduction of aluminous ferric iron to bridgmanite stabilises the bridgmanite phase despite the ferric iron occupying the A site rather than the B site and having no spin transition and no dependence of the transition pressure on the value of U_{eff}.

There are additional problems to finding the effect of ferric iron on the relative phase stabilities. As the dE/dP values of bdg and ppv are so similar the effects of iron clustering and temperature may be very important. As outlined below different arrangements of ferric iron in bdg lead to quite different energies and spin- and as the U_{eff} variations show different spin values in ferric iron can lead to highly varied transition pressures. In this work we have placed the ferric iron in its most stable positions but variations in the configurational entropy and magnetic entropy (based on the favourability of distributing iron across different lattice site) may significantly change the transition pressure once more and this needs careful examination.

Thus the effect of ferric iron on the bdg-ppv transition is theoretically unclear. Strictly speaking comparisons of the energy between different systems (such as bdg vs ppv) require a single equal value of U_{eff} in the two different systems (as when we apply U_{eff} = 3.0) but practically variant U_{eff} values do not cause systematic shifts in energy which we confirmed with our own data. Ultimately more work needs to be done to carefully tease apart these effects but the self-consistent U_{eff} values are likely a better reflection of the electronics of ferric iron and they agree with the experimental data (Gialampouki et al., 2018; Piet et al., 2016) that suggests ferric iron does not like to reside in ppv. Thus it is likely that ferric iron stabilises the bdg phase considerably and thus ferric-iron enriched bridgmanite should be in the bdg phase at the CMB. If ppv is formed at the CMB-either in a one phase or two phase region- it is unlikely to contain much ferric iron as this iron can partition to other phases and so ferric iron effects on ppv elasticity are likely unimportant. Therefore in this work we shall consider only the bdg phase for the rest of the work.

We can speculation, however, on how ferric iron in the ppv phase would behave. To address this possibility- that ferric iron bridgmanite is in the ppv phase at the CMB- we calculated the effect of ferric iron on the static elasticity of bdg and ppv at 136 GPa (Table S1). Iron has near identical effects on the bdg and ppv phase as can be seen by the conversion from bdg to ppv which causes a negligible change in P velocity and a 2% decrease in S velocity regardless of if iron is present or not. This means that the results considered below likely also apply in a ppv dominant regime but all shear velocities will be scaled down by ~2% which will cause slight improvements in fitting to ULVZ values. This is in contrast to aluminous Fe iron which has quite different elasticities in the bdg and the ppv phase but this is due to the Fe and Al atoms swapping sites on conversion from bdg to ppv (Caracas, 2010).

3.2. Spin states

Before the elasticity can be calculated the stable spin structure of ferric iron bridgmanite must be known. Fig. 1 shows the variation in percentage of iron in a low spin state for $Fe_{0.5}Mg_{0.5}Fe_{0.5}Si_{0.5}O_3$ as a function of pressure at different temperatures, where the free energies used in Eq. 1 are calculated using thermodynamic integration (TI). We also compare this to a simpler method that only combines static enthalpy and magnetic entropy effects and ignores the vibrational entropy contribution. The latter method produces distributions of iron spin that are very close to those produced by the TI method at 2000 K and shows

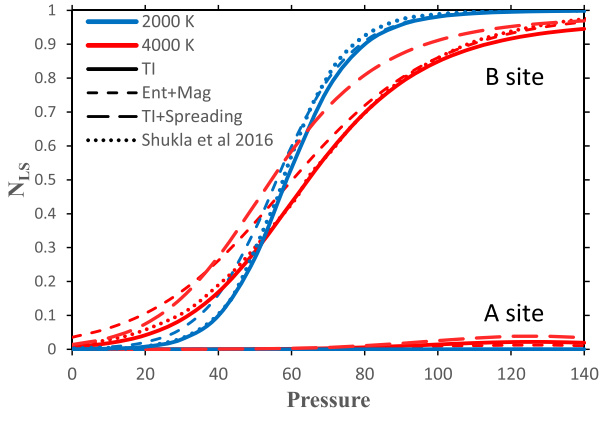

Fig. 1. N_{LS} ($N_{LowSpin}/N_{Total}$) in the A and the B site of $Fe_{0.5}Mg_{0.5}Fe_{0.5}Si_{0.5}O_3$ as a function of pressure at temperatures of 2000 and 4000 K. The solid lines were calculated with thermodynamic integration (including magnetic entropy), the short dashed lines are without vibrational entropy (enthalpy + magnetic entropy only), and the dotted lines are from Shukla et al., 2016. At high temperatures thermal spreading of the electrons removes the magnetic entropy differences between "high" and "low" spin states and this effect is shown with long dashed lines for 4000 K. Significant numbers of low spin iron are not created in the A site under these conditions and only at high pressure and temperature can small changes be seen. At the CMB iron is mostly high spin in the A site and low spin at the B site.

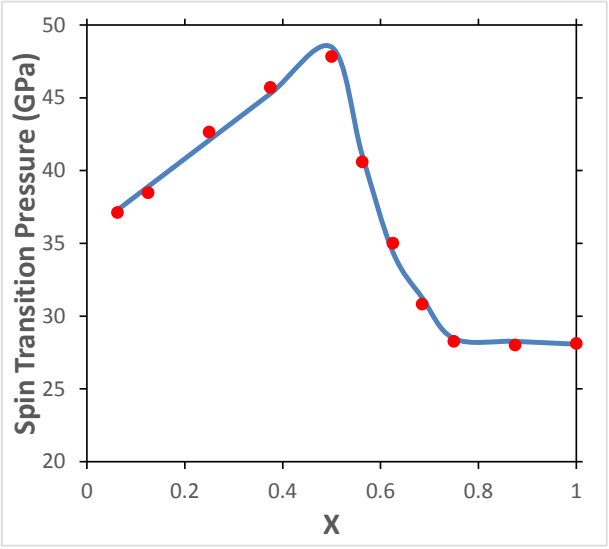

Fig. 2. Graph showing the calculated static spin transition of $Fe_{2x}Mg_{1-x}Si_{1-x}O_3$ (red points) showing a strong non-linear effect of the concentration of Fe. These points were calculated with the most stable arrangement of iron in $Fe_{2x}Mg_{1-x}Si_{1-x}O_3$ which has the A site iron at maximum seperation along [110] rows and B site iron at the closest site to the A site iron. The highly non-linear trend of the spin transition with concentration is because the spin transition pressure of each iron atom is dependant on how many next nearest iron neighbours it has (0, 1, 2 or 4). In this most stable configuration each iron starts with 0 iron neighbours and increases to 4 as concentration increases. The effect of this is shown with the blue line which is a simple spin transition model based on the amount of iron neighbours each iron has and was constructed independently of the data in this plot but reasonably replicates it. For details of its construction see supplementary methods and for other iron arrangements see Fig. S2. However, except for very high Fe contents, the spin transition has completed well before ULVZ conditions and so this does not impact our results here. (For interpretation of the references to colour in this figure legend, the reader is referred to the web version of this article.)

that the effects of vibrational entropy on spin state are very small at typical lower mantle temperatures. Only when the temperature increases to near CMB temperatures (~4000 K) does this assumption start to breakdown but even then the magnetic entropy term is overwhelmingly the most important term.

No spin transition was seen at A site for pressures within the Earth's mantle whereas B site ferric iron has a transition at middling lower mantle pressures. Fig. 2 shows the variation in the static spin transition pressure at the B site with varying iron content ($Fe_{2x}Mg_{1-x}Si_{1-x}O_3$) and Table 2 shows the variation in entropy with iron content at lower mantle conditions (the spin state of bridgmanite with variable iron concentration along a geotherm is shown in Fig. S1). This is different to ferropericlase where a linear trend of spin transition pressure with ferrous iron content is seen (Muir and Brodholt, 2015a) but a compositional dependence on spin transition pressure has been previously predicted with ferrous iron in bridgmanite -Bengtson, 2008 #1057_. It is seen that increasing the iron content initially (up to x = 0.5) increases the spin transition pressure and then it decreases with increasing iron content until it reaches a plateau at very high iron contents. This is because the iron spin transition depends upon both the concentration of the iron and its local environment. The effect of local iron environment can be seen in Fig. S2 where we show that different arrangements of iron in an x = 0.5 system (such as by forming layers in the AB plane or clusters of iron where the iron is placed as close as possible to each other in one half of the crystal) can change the spin transition by up to 20 GPa. This variation in spin transition due to iron arrangement is of similar magnitude to the variations seen in experimental estimates of the spin transition pressure of B site ferric iron and it is also similar to our calculated pressure variations of the spin transition that are caused by changing the iron content. This latter point means that when considering theoretically the spin transition in ferric iron sampling only the most stable arrangement is likely not sufficient and that one needs to sample the full distribution of possible iron arrangements and also that sluggish iron diffusion in bridgmanite may lead to small variations of the spin transition pressure experimentally. However, except for very high Fe contents, the spin transitions in the B-site iron have completed well before ULVZ conditions (Fig. 1 and S1) and so the effect of the exact atomic arrangement on the spin transition pressure does not impact the results here.

In general, DFT calculations performed without fixing the spin produce structures with a high spin A site and a low spin B site at lower mantle pressures. Resultant spins from these calculations are listed for 0 and 4000 K in Table 3 (and 2000 K listed in Table S2). An exception is produced, however, at 4000 K, where the most stable states produced by unfixed spin polarised runs were HS-HS. This is not due, however, to

Table 2
Table showing the spin transition pressure (calculated at static conditions), entropy change upon going from a high to a low spin state (at 136 GPa and 4000 K), the Clapeyron slope of the spin transition pressure for A and B site ferric atoms in $Fe_{2x}Mg_{1-x}Si_{1-x}O_3$ and the proportion of iron that would be low spin at 136 GPa and 4000 K (N_{LS}).

x	Transition (GPa)	dS (eV)	dS/dV (eV/Å^3)	N_{LS} 2000 K
A site				
0.25	> 200	−9.41	0.010	0.00
0.5	> 200	−10.07	0.011	0.03
0.75	> 200	−10.11	0.012	0.18
1	176	−10.11	0.012	0.33
B Site				
0.25	45	−0.73	0.001	0.98
0.5	48	−1.39	0.001	0.97
0.75	28	−1.42	0.001	0.99
1	28	−1.43	0.001	0.99

Table 3
Average absolute spin (S) of ferric iron in the A or B site, and unit cell parameters of $Fe_{2x}Mg_{1-x}Si_{1-x}O_3$ with varying pressure. These are given at 0 K and 4000 K for spin polarised and spin fixed results, where the first value is the high spin case and the second value is the low spin case. The 30 GPa and 0 K state is a metastable state shown for comparison. 2000 K cell parameters are presented in Table S2.

	X = 1					X = 0.5	X = 0.25
0 K	30 GPa	60	90	136	150	136	136
Spin of A	2.49	2.46	2.43	2.39	2.38	2.50	2.50
Spin of B	0.66	0.63	0.61	0.57	0.56	0.50	0.50
Vol (Å^3)	164.3	155.1	146.2	132.8	129.3	128.1	125.3
B/A	0.93	0.91	0.89	0.85	0.85	0.89	0.92
C/(√2A)	0.97	0.96	0.94	0.91	0.90	0.94	0.96
Vol Fixed (Å^3)	180.0/ 153.4	168.7/ 145.8	158.0/ 138.2	142.2/ 127.3	137.5/ 125.1	132.3/ 124.7	127.2/ 123.5
B/A Fixed	0.96/ 0.97	0.94/ 0.97	0.91/ 0.96	0.87/ 0.95	0.86/ 0.95	0.89/ 0.94	0.91/ 0.90
C/(√2A) Fixed	0.99/ 0.98	0.97/ 0.97	0.96/ 0.97	0.93/ 0.96	0.92/ 0.96	0.95/ 0.96	0.96/ 0.95
4000 K	30 GPa	60	90	136	150	136	136
Spin of A	2.19	2.06	1.92	1.72	1.65	1.7	1.51
Spin of B	2.14	2.01	1.88	1.65	1.58	1.7	1.51
Vol	174.3	163.0	152.6	138.3	134.3	132.4	129.6
B/A	0.92	0.91	0.89	0.86	0.84	0.90	0.92
C/(√2A)	0.97	0.96	0.95	0.92	0.91	0.95	0.96
Vol Fixed (Å^3)	194.8/ 169.8	180.1/ 158.2	166.0/ 147.2	147.7/ 133.3	139.6/ 126.7	137.3/ 129.6	131.7/ 128.1
B/A Fixed	0.97/ 0.99	0.93/ 0.98	0.90/ 0.98	0.85/ 0.98	0.83/ 0.98	0.88/ 0.95	0.89/ 0.93
C/(√2A) Fixed	1.01/ 0.99	0.98/ 0.98	0.95/ 0.98	0.91/ 0.97	0.89/ 0.96	0.93/ 0.96	0.93/ 0.96

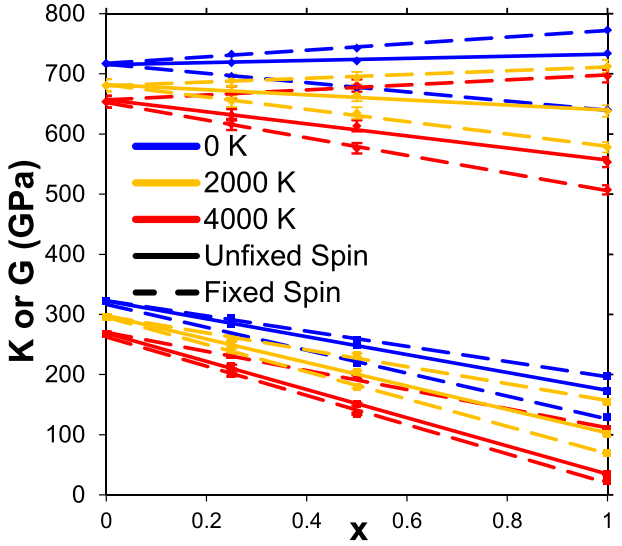

Fig. 3. Plot showing the effect of spin on the VRH bulk and shear modulus of $Fe_{2x}Mg_{1-x}Si_{1-x}O_3$ bridgmanite as a function of Fe^{3+} at 136 GPa and 0 K, 2000 K and 4000 K. Solid lines are unfixed spin polarised results, dashed lines are runs with spin fixed as either HS or LS in both sites, with the smaller values always being the HS-HS system. The statisical error of the MD runs is represented by error bars but is below < 1.5% for all systems and is too small to observe for the G at this scale.

a traditional "spin transition" at the B site as the volume, B/A ratio and $c/\sqrt{2}A$ ratios of the unit cell are more compatible with the HS-LS structure rather than a HS-HS structure at the same temperature (see Table 2). Instead this is simply due to the thermal spreading of electrons at the B site which repopulate the high spin state as the band gap reduces relative to kT (predicted bandgaps via PDOS are shown in Table S3). The difference in bandgap between the A and the B site also reduces relative to kT and so with increasing temperature thermal spreading at both sites becomes dominant and the magnitude of their spins become increasingly equal despite the large geometric and band structure differences between two sites. Nevertheless, at 4000 K unfixed spin polarised runs reproduce a ferric iron bridgmanite that has the geometry, and thus as seen below the elasticity, of a HS-LS structure at that temperature and so this change in the spin structure of the B site will not produce elastic differences (compared to a pure HS-LS structure) and thus will not produce seismically observable differences even at the CMB.

3.3. Elastic constants and velocity

Fig. 3 shows the variation in G and K with ferric iron content and temperature at 136 GPa (values at lower pressure are given in Table S4 and shown in Fig. S3). The individual elastic constants are given in Table S5–S6.

We find that adding ferric iron linearly decreases G for all spins although the magnitude of the effect is greater with high spins compared to low spins. At the CMB temperature (~4000 K) the shear modulus of the mixed HS-LS state is nearer to the HS-HS state than it is to the LS-LS state and thus at the CMB the spin state of B has only a small effect on G.

The effect on K is more complicated since the addition of ferric iron can increase or decrease K depending upon the spin state. At all temperatures we find that the LS-LS state increases K while the HS-HS state decreases K. Again, the mixed spin state falls between the HS-HS and LS-LS cases. At the temperatures of ULVZs, we find that the bulk-modulus of the HS-LS state is nearer to the HS-HS state as was also seen with G. So the spin state of the A site is again the largest control on elasticity and a spin transition in A would have a large effect but this only occurs at pressures much greater than in the Earth's mantle.

The effect of ferric iron on the bulk modulus has been examined experimentally with different results. Some studies show the ferric iron can increase K and some a decrease, with a dK/dFe% ranging from −4 to +5 with no obvious trends with iron/aluminium content or pressure (Andrault et al., 2001; Dorfman and Duffy, 2014; Nishiyama et al., 2007; Nishio-Hamane et al., 2008; Saikia et al., 2009; Ballaran et al., 2012; Catalli et al., 2011; Catalli et al., 2010; Kurnosov et al., 2017). These differences have been attributed to a variety of factors such as oxidation state, different site occupations of Fe, different pressure ranges to account for the spin transition, different amounts of Aluminium and a lack of precision in high pressure measurements (Saikia et al., 2009). We predict a relatively small effect of iron on K the sign of which is dependent on both spin state and temperature. At 0 GPa and 0 K we find dK/dFe% = −0.65 and dG/dFe% = −1.03, similar to that found in Shukla et al. (2016) of −0.48 and − 1.00. In the lower mantle and particularly at the CMB dK/dFe% should always be negative. HS-HS states always have a negative dK/dFe% and HS-LS states will have a negative dK/dFe% at lower mantle temperatures.

The large decrease in G, together with the increase in density on going from $MgSiO_3$ to Fe_2O_3 produces large decreases in seismic velocities (Fig. 4). At CMB conditions and if large amounts of ferric iron are present some B sites becomes HS due to the increased temperature (as seen in Fig. 1) and this causes a slight decrease in V_p and a slight increase in V_s as shown by the dotted line in Fig. 4.

3.4. Velocities of bridgmanite containing both ferrous and ferric iron

To consider the coeffect of Fe^{2+} and Fe^{3+} in bridgmanite, we examined a series of structures of $Fe_{x+y}Mg_{1-x}Si_{1-y}O_3$, where x + y = 0.5 ($Fe_{0.5}Mg_{0.5}SiO_3$, $Fe_{0.5}Mg_{0.5625}Si_{0.9375}O_3$, $Fe_{0.5}Mg_{0.625}Si_{0.875}O_3$, $Fe_{0.5}Mg_{0.6875}Si_{0.8125}O_3$ and $Fe_{0.5}Mg_{0.75}Si_{0.75}O_3$). Different geometries

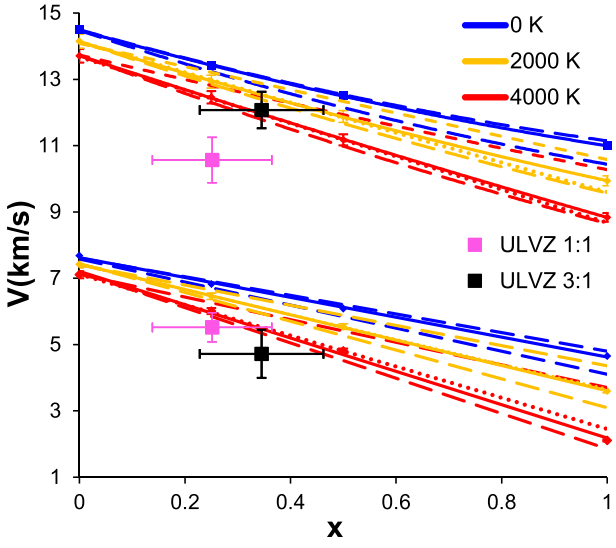

Fig. 4. VRH averaged V_p (larger values) and V_s of $Fe_{2x}Mg_{1-x}Si_{1-x}O_3$ at 136 GPa and 0, 2000 and 4000 K. Solid lines are unfixed spin polarised results, dashed lines are runs with fixed HS-HS or LS-LS spins, with the smaller values always being HS-HS runs. The statisical error of the MD runs is represented by error bars but all are below < 1.5% and cannot be easily seen. Dotted lines represent the expected velocities taking into account HS/LS mixing on the A and B site. The black points are 3:1 ULVZ values. These were determined by modifying PREM velocities at the CMB with a typical range of observed ULVZ values (ρ +5–15%, V_p −8-15%, V_s −24-45%). The value for x is chosen to match the density. The pink points show the most favourable parameters observed in Brown et al., 2015 (ULVZ 1:1) (ρ +6%, V_p − 23%, V_s − 24%). Bridgmanite containing purely ferric iron touches the outer edges of the black points but cannot fit the Brown et al. data. (For interpretation of the references to colour in this figure legend, the reader is referred to the web version of this article.)

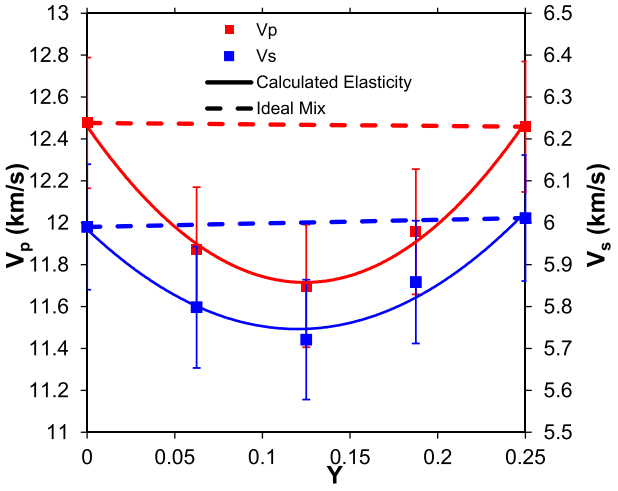

Fig. 5. VRH averaged V_p (red, left axis) and V_s (blue, right axis) of bridgmanite at 136 GPa and 4000 K with compositions of $Fe_{x+\ y}Mg_{1-x}Si_{1-y}O_3$, where x + y always equals 0.5. y = 0 corresponds to a composition where all iron is Fe^{2+} and y = 0.25 corresponds to a composition where all iron is Fe^{3+}. The solid line is a fit to our calculated values while the dashed line is a *Hashin-Shtrikman* mixture of isolated ferric and ferrous endmembers - the velocity bounds of this mixture are so similar that they appear as one line. There is a strong decrease in V_p (and smaller decrease in V_s) when mixing ferric and ferrous iron in bridgmanite. (For interpretation of the references to colour in this figure legend, the reader is referred to the web version of this article.)

of iron were tested but the most enthalpically stable ferrous/ferric arrangements were the same as the most stable ferric iron arrangements and these were used to determine the elasticity. This sees the iron atoms organised in [110] rows and the A-site ferric iron close to the B-site ferric iron. In all runs the ferric and ferrous iron remained magnetically independent- ferric iron remained ferric and ferrous iron remained ferrous without hybrid iron states forming.

Fig. 5 (elastic constants in Table S3) shows the calculated elasticity of the ferric/ferrous mixed structures at 136 GPa at 4000 K. We find that the elasticity of bridgmanite containing both ferric and ferrous iron differs strongly from the Hashin-Shtrikman (H−S) (Davies, 1974) mixture of the end-members. Both V_p and V_s are lowest when the ferric:ferrous ratio is approximately 1:1, rather than when it is entirely ferric as would be predicted from an ideal mixture. For bridgmanite containing 50% iron, this non-linear mixing decreases V_p by as much as 0.5–1 km/s from the H−S prediction. It also has the effect of strongly decreasing $dlnV_s/dlnV_p$ of these iron systems compared to $MgSiO_3$. For CMB conditions $dlnV_s/dlnV_p$ changes from 1.56 when all the iron is ferric to 1.27 when half of the iron is ferric, and to 1.61 when all the iron is ferrous. Such an effect has also been seen experimentally by Ismailova et al., 2016 where a significant decrease in K was observed with a mixed ferrous-ferric composition. It should be noted that many experiments do not measure simultaneously the ferric:ferrous ratio and the elasticity and so this effect will often not be measured. We also performed these calculations at 80 GPa and 2000 K and saw similar effects (Fig. S4) and a similar percentage decrease in V_p and V_s as when the calculation is performed at 136 GPa and 4000 K. This effect is thus not limited to CMB pressures and temperatures and is likely a factor throughout mantle conditions if sufficient ferric iron is present alongside ferrous iron. This effect is particularly significant when ferric iron makes up 20–80% of the total iron content.

4. Geophysical implications

Ferric iron was found to behave largely like ferrous iron in the mantle. In Fig. S5 we plot the velocities of ferric containing bridgmanite across a lower mantle geotherm and these results are similar to those of ferrous containing bridgmanite (Wentzcovitch et al., 2010) outside of a small discontinuity at ~40–80 GPa caused by the B site spin transition. Such a result was also found by Shukla et al. (2016) and for Yu et al. (2012) in ppv. Thus for most of the lower mantle ferric iron will cause no variations in seismic behaviour beyond that induced by ferrous iron. A key difference, however, comes from the large discontinuity that we observed with mixed ferric and ferrous iron which would cause seismically relevant effects and seemingly occurs independent of pressure and temperature. This effect needs to be studied either experimentally or with a careful theoretical method because as shown in Fig. 5 the errors bars on our seismic velocity estimate are nearly as large as the size of our effect and the effects of any phase change need to be properly accounted for. Regardless, we found that this effect is only strongly significant when ferric iron accounts for middling amounts of ferric iron (~10–90%) of the total iron concentration but thermodynamic modelling suggests that most of the lower mantle should contain much lower concentrations of ferric iron than this (Xu et al., 2015) and thus it can be discarded as an important effect in most regions of the lower mantle. In regions with large amounts of iron -such as potentially ULVZs- this could be a very important effect, however, and so we shall examine these effects in ULVZs.

ULVZs are regions that maybe highly enriched in iron. The $\Sigma Fe^{3+}/\Sigma Fe^{Total}$ ratio in highly enriched iron samples is poorly studied though recently it has been shown that an iron-end member of bridgmanite with high quantities of ferric iron (~34%) is stable to deep in the mantle (Ismailova et al., 2016). Since the amount of iron required to explain ULVZs greatly exceeds the amount of Al, Al should not be a strong control on ferric iron content. Energetic calculations suggest that in such a situation the ferric iron content is expected to be low (< 0.2) (Xu et al., 2015) and correlations between iron content and $\Sigma Fe^{3+}/\Sigma Fe^{Total}$ ratio have not been observed (Boujibar et al., 2016). Thus it is likely that < 20% of iron will be ferric in high iron bridgmanite though as Ismailova et al., 2016 demonstrates significant uncertainties remain.

Fig. 6 compares the velocities and densities of bridgmanite with varying ferric:ferrous ratios to those observed in ULVZs. We have considered both ULVZs where the reduction of V_s to V_p is about 3:1 and the recent observation of a ULVZ with far greater reduction in V_p (Brown et al., 2015). As can be seen the velocities of bridgmanite with entirely ferric and entirely ferrous iron are very similar. As such, bridgmanite with either x = 0.74–0.83 ferrous iron ($Fe_xMg_{1-x}SiO_3$) or y = 0.38–0.45 ferric iron ($Fe_{2y}Mg_{1-y}Si_{1-y}O_3$) is able to fit the properties of 3:1 ULVZs. This agrees with our previous work on ferrous iron bearing bridgmanite (Muir and Brodholt, 2015a). However, this is not the case for the 1:1 ULVZs which have very large reductions in V_p. Bridgmanite with solely ferrous iron or ferric iron cannot produce such a large reduction in V_p.

Also shown in Fig. 6 is that the non-linear mixing of ferric and ferrous iron shown in Fig. 5 changes the situation significantly. Even small amounts of mixing between ferric and ferrous iron substantially reduces V_p such that bridgmanite is unable to fit the properties of 3:1 ULVZs when the ferric:ferrous ratio exceeds ~10% (or is below ~90%) with even a 5% ratio substantially reducing the range of possible fits. On the other hand, the strong decrease in V_p improves the fit to the properties of 1:1 ULVZs. Thus non-linear mixing of ferric and ferrous iron in bridgmanite has large seismic effects in these conditions. In the pure bridgmanite case very low amounts of ferric iron are expected to occur energetically and thus there should be no strong V_p decrease and the properties of 3:1 ULVZs can be fit (using mostly ferrous iron) and the properties of 1:1 ULVZs cannot be fit.

Bridgmanite is not alone in the lower mantle and thus we shall also consider ULVZs made of bridgmanite and ferropericlase. As shown in Muir and Brodholt (2015a), a mixture of ferrous iron-bearing bridgmanite and ferropericlase can substantially improve the fitting to 3:1 ULVZ properties. We shall examine how ferric iron changes this picture. There is a wide parameter space to explore and fitting to ULVZ properties was done as in Muir and Brodholt (2015a). 4 key parameters are

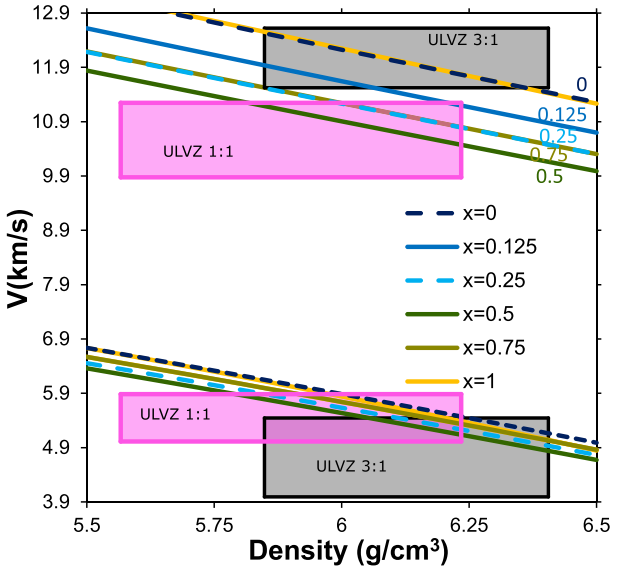

Fig. 6. VRH-averaged velocities of bridgmanite with increasing amount of iron (as measured in the density) and different ferric/ferrous ratios, x = $\Sigma Fe^{3+}/\Sigma Fe^{Total}$. Results are given at 136 GPa and 4000 K. Also shown are values for ULVZs. Grey is the normal range of ULVZs where $dlnV_s/dlnV_p = 3$ and pink is a more recent observation where changes in V_p are much greater and $dlnV_s/dlnV_p = 1$ (Brown et al., 2015). Acceptable compositions that fit 3:1 ULVZ properties are when V_p and V_s fall within the grey box at the same density. Similarly for 1:1 ULVZs, V_p and V_s must fall within the pink box at the same density. 3:1 ULVZs can be fit with either ferrous or ferric iron enriched bridgmanite, but the non-linear effect on V_p of even small amounts iron with the other oxidation state degrades the fit significantly. On the other hand, 1:1 ULVZs cannot be modelled with bridgmanite with just ferric or ferrous iron and needs to have iron in both oxidation states to achieve a fit. (For interpretation of the references to colour in this figure legend, the reader is referred to the web version of this article.)

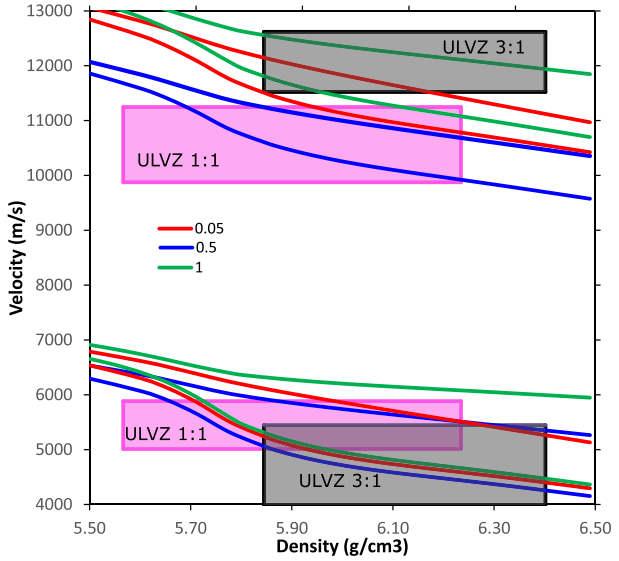

Fig. 7. The velocities of an example ferropericlase-bridgmanite mixture compared to ULVZ properties at 136 GPa and 4000 K. The Fe partitioning ($K = \frac{x_{fp}^{Fe}/x_{fp}^{Mg}}{x_{bd}^{Fe}/x_{bd}^{Mg}}$) is fixed at 0.005 and the ferropericlase to bridgmanite ratio to 15:85 (both values chosen as particularly good fit values for a ferrous bridgmanite:fp mixture but variation does not cause major changes as shown in Muir and Brodholt, 2015a). 3 different values of $\Sigma Fe^{3+}/\Sigma Fe^{Total}$ are shown, with all ferric iron in the bridgmanite. The two lines for each ferric iron concentration are the Hashin-Shtrikman bounds; these are large due to the very low G in iron-enriched ferro-periclase. The 100% ferric iron case is shown to demonstrate the case without mixing; the 0% ferric iron case is not show but is very similar to the 100% one. The 5% case is a possible system that is mostly ferrous iron with only a small amount of ferric iron, and shows how even small amounts of mixing makes the fit to 3:1 ULVZ properties much worse. The 50% case shows that the 1:1 ULVZ properties can easily be fit by a mixture of fp and bd with half the iron in bridgmanite as ferric. An alternative fitting is shown in Fig. S6.

present- the amount of iron, the ferropericlase:bridgmanite ratio, the partitioning of iron between bridgmanite and ferropericlase and the ratio of ferric:ferrous iron in bridgmanite. The first 3 of these parameters were explored in the previous paper, here we shall explore the 4th. Thus we shall take the conclusions of Muir and Brodholt (2015a) and see how varying the ferric:ferrous ratio (while keeping the other 3 parameters fixed to those results) affects the V_p, the V_s and the density of our theoretical mixture and how this variation in parameters fits within the experimental observation windows of ULVZs.

In the case of entirely ferric iron-containing bridgmanite, which has very similar velocities to ferrous-containing bridgmanite, we find essentially the same conclusions as in Muir and Brodholt (2015a). In other words, ULVZ properties are accurately modelled by a mixture of ~80% bridgmanite and ~ 20% ferropericlase, where iron is partitioned strongly into the ferropericlase phase, regardless of whether the iron is ferric or ferrous and a wide range of parameters can fit the seismic properties into the 3:1 ULVZ windows. The 3 variables not related to ferric iron- bdg:fp ratio, total amount of iron and partitioning between fp and bdg have essentially the same tradeoffs as was seen in Muir and Brodholt (2015a). The best fits are again achieved by partitioning most of the iron to feropericlase. This sense of partitioning is thermodynamically viable in cases where Al^{3+} does not play an important role (Muir and Brodholt, 2016). While there is a difference in partitioning to ferropericlase between ferric and ferrous iron (Gialampouki et al., 2018; Piet et al., 2016) in both cases the ferropericlase takes the majority of the iron and as was shown in Muir and Brodholt (2015a) small variations in the partitioning number have little effect on the mixture. The exact best fits (i.e. when modelled properties are nearest to the middle of the range of 3:1 ULVZ V_p, V_s and densities simultaneously) are $0.88Fe_{0.35}Mg_{0.65}SiO_3$ + 0.12FeO with ferrous iron bridgmanite and $0.86Fe_{0.185}Mg_{0.815}Fe_{0.185}Si_{0.815}O3$ + 0.14FeO with ferric iron bridgmanite. There is, however, a wide array of other compositions which can give similarly good fits and the variation in fitting with varying the parameters is essential the same as with ferrous iron shown in Muir and Brodholt (2015a). Essentially entirely ferric iron compositions do not impair fitting to 3:1 ULVZ properties.

An unconsidered factor in those calculations, however, was the ferric:ferrous ratio. Fig. 7 shows V_p, V_s and density of iron-containing bridgmanite compared to ULVZs for a sample case with 15% ferropericlase and 85% bridgmanite (chosen because it has a particular good fit with ferrous only bridgmanite and is close to a pyrolitic value). As can be seen, the 3:1 ULVZs can be easily explained by a mixture of bridgmanite and ferropericlase with either all ferric or all ferrous iron (or if ferric and ferrous iron do indeed mix linearly in bridgmanite). However, even small amounts of mixing of ferric and ferrous iron in bridgmanite strongly reduces the bridgmanite V_p and, therefore, the fit to 3:1 ULVZ properties. With 5% ferric iron the parameter window which reproduces 3:1 ULVZ properties is substantially reduced as is the window of 3:1 seismic velocities that can be reached by that parameter window.

This is explored in more detail in Fig. S6 where the parameter space is allowed to vary but in general we find that for the 3:1 ULVZs fitting to properties is substantially reduced by adding any ferric iron to bridgmanite. Substantially no solutions can be found that replicate 3:1 ULVZ properties when bridgmanite contains 35–55% ferric iron. Conversely adding any ferric iron to bridgmanite improves fitting to the 1:1 ULVZ properties and bridgmanite with 20–80% ferric iron provides the best

fits.

Ultimately, however, for a ferric or ferrous bridgmanite there are many parameters that can reproduce 3:1 ULVZ properties but not 1:1 ULVZ properties and for a ferric:ferrous mixture that are many parameters that can reproduce 1:1 ULVZ but not a 3:1 ULVZ properties. Using the conclusion of Xu et al. (2015) that ferric iron should make up < 20% of iron in bridgmanite (and often quite a bit less) in this region both the properties of 3:1 and 1:1 ULVZs can be fit by a bridgmanite:ferropericlase mixture but ferric iron makes the fitting to the 3:1 ULVZ worse.

We stress that essentially ferric iron makes no difference to ferrous iron when considering the seismic properties of bridgmanite but in situations where there is a middling amount of ferric and ferrous iron then strong seismic variations are seen. Thus the ratio of ferric iron to ferrous iron in bridgmanite is a very important thermodynamic parameter which needs to be reliably known when considering seismic properties.

An unconsidered factor in this calculation is the presence of aluminium in the bridgmanite. Computations (Wang et al., 2015; Shukla et al., 2016; Zhang et al., 2016) have suggested that the elasticities of $FeSiO_3$, $FeAlO_3$ and Fe_2O_3-bearing bridgmanite are very similar outside of spin crossover regions though other calculations suggest considerable differences between aluminous ferric iron and ferrous iron (Caracas, 2010). A recent set of XRD and Brillouin spectroscopy experiments (Kurnosov et al., 2017) suggest that $FeAlO_3$ bearing bridgmanite has significantly reduced seismic velocities when compared to $FeSiO_3$ and Fe_2O_3 bearing bridgmanite while other XRD studies (Ballaran et al., 2012; Catalli et al., 2011) suggests that $FeAlO_3$ causes a more modest change to seismic velocities than $FeSiO_3$ or Fe_2SiO_3. Some difficulties remain with fitting these experimental results to pressure as the results of Kurnosov et al. (2017) only extend to 40 GPa whereas the work of Ballaran et al. (2012) found that significantly different elasticity results were obtained when fitting modulus data above and below 40 GPa. Ultimately more work is needed to untangle the coeffect of ferrous, ferric, aluminium and spin transition on bridgmanite elasticities. Most data shows that $FeAlO_3$ has only a modest effect on the elasticity of bridgmanite. While Kurnosov et al. (2017) shows a large effect of $FeAlO_3$ the shear velocities of their different compositions of Fe and Al containing bridgmanite systems seem to converge at 40 GPa which would suggest that the shear velocities of $FeAlO_3$ containing bridgmanite and Fe or Al or Mg containing bridgmanite are similar at high pressures. Shear velocities are the strongest control on ULVZ fitting and thus if $FeAlO_3$ has similar shear velocities to $FeSiO_3$ and Fe_2O_3 at high pressures then the presence of $FeAlO_3$ will not change the elasticities calculated here. Aluminium can affect the distribution and charge of iron but some of our fits to 3:1 ULVZ properties contain very large amounts of iron (> 30%) in bridgmanite and thus the properties of iron should not be controlled by the smaller amounts of aluminium that maybe present. In the case of fitting to the 1:1 ULVZs some of the best fitting mixtures have bridgmanite with very small amounts of iron (< 1%) which would be affected by the presence of aluminium but there are valid solutions with bridgmanite containing large amounts of iron (> 25%). Thus the presence of Al does not prevent ferric-ferrous containing bridgmanite from forming solutions with ferropericlase that have the seismic properties of ULVZ regions in either the 3:1 or the 1:1 case.

5. Conclusion

Ferric iron, similar to ferrous iron, substitution into brigmanite causes a large decrease in seismic velocities. At CMB conditions, V_s and V_p for Fe_2O_3 are respectively 74% and 36% lower than those of $MgSiO_3$. The decrease in both velocities is linear with iron concentration. As with the elastically similar ferrous iron-enriched bridgmanite, ferric iron-enriched bridgmanite can also fit the properties of some ULVZs (those with dlnVs/dlnVp = 3). The fit to these ULVZ properties improves with the addition of ferropericlase. On the other hand, ULVZs which have a much greater reduction in V_p (ie. $d\ln V_s/d\ln V_p = 1$) as seen in Brown et al., 2015, cannot be modelled with bridgmanite with just ferric or ferrous iron. However, the velocities of bridgmanite containing both ferric and ferrous iron are not ideal, and instead the mixing of ferric and ferrous iron produces much larger decreases in V_p than expected. This non-ideality makes it impossible to fit a bridgmanite-ferropericlase mixture to 3:1 ULVZ properties if both ferrous and ferric iron are present in equal amounts and makes the fitting to properties worse with any small amount of ferric iron. On the other hand, the properties of 1:1 ULVZs are much better fit by a mixture of both oxidation types. The effect of ferric and ferrous mixing, ferric iron clustering in bridgmanite and post-perovskite and the oxidation state of iron in bridgmanite thus need to be better studied.

CRediT authorship contribution statement

Joshua M.R. Muir:Methodology, Investigation, Formal analysis, Writing - original draft.**John P. Brodholt**:Conceptualization, Supervision, Project administration, Funding acquisition, Writing - review & editing.

Declaration of competing interest

The authors declare that they have no known competing financial interests or personal relationships that could have appeared to influence the work reported in this paper.

Acknowledgements

The research in this proposal was supported by NERC Grants NE/H021027/1 and NE/M00046X/1. Calculations were run on the UK National HPC facility, ARCHER. The authors would like to thank the many helpful reviewers that suggested improvements to this work.

Appendix A. Supplementary data

Supplementary data to this article can be found online at https://doi.org/10.1016/j.pepi.2020.106505.

References

Akber-Knutson, S., Steinle-Neumann, G., Asimow, P.D., 2005. Effect of Al on the sharpness of the MgSiO3 perovskite to post-perovskite phase transition. Geophys. Res. Lett. 32.

Andrault, D., Bofan-Casanova, N. & Guignot, N. 2001. Equation of state of lower mantle (Al,Fe)-$MgSiO_3$ perovskite. Earth Planet. Sci. Lett., 193, 501–508.

Andrault, D., Munoz, M., Bolfan-Casanova, N., Guignot, N., Perrillat, J.-P., Aquilanti, G., Pascarelli, S., 2010. Experimental evidence for perovskite and post-perovskite coexistence throughout the whole D″ region. Earth Planet. Sci. Lett. 293, 90–96.

Ballaran, T.B., Kurnosov, A., Glazyrin, K., Frost, D.J., Merlini, M., Hanfland, M., Caracas, R., 2012. Effect of chemistry on the compressibility of silicate perovskite in the lower mantle. Earth Planet. Sci. Lett. 333, 181–190.

Boujibar, A., Bolfan-Casanova, N., Andrault, D., Bouhifd, M.A., Trcera, N., 2016. Incorporation of Fe2+ and Fe3+ in bridgmanite during magma ocean crystallization. Am. Mineral. 101, 1560–1570.

Bower, D.J., Wicks, J.K., Gurnis, M., Jackson, J.M., 2011. A geodynamic and mineral physics model of a solid-state ultralow-velocity zone. Earth Planet. Sci. Lett. 303, 193–202.

Brown, S.P., Thorne, M.S., Miyagi, L., Rost, S., 2015. A compositional origin to ultralow-velocity zones. Geophys. Res. Lett. 42, 1039–1045.

Bykova, E., Dubrovinsky, L., Dubrovinskaia, N., Mccammon, C., Ovsyannikov, S.V., Liermann, H., Kupenko, I., Chumakov, A., Ruffer, R., Hanfland, M., Prakapenka, V., 2016. Structural complexity of simple Fe_2O_3 at high pressures and temperatures. Nat. Commun. 7, 10661.

Caracas, R., 2010. Elasticity of AlFeO3 and FeAlO3 perovskite and post-perovskite from first-principles calculations. Geophys. Res. Lett. 37, L203061–L203065.

Caracas, R., Cohen, R.E., 2005. Effect of chemistry on the stability and elasticity of the perovskite and post-perovskite phases in the $MgSiO_3$-$FeSiO_3$-Al_2O_3 system and implications for the lowermost mantle. Geophys. Res. Lett. 32, L163101–L163104.

Catalli, K., Shim, S.-H., Prakapenka, V., 2009. Thickness and Clapeyron slope of the post-perovskite boundary. Nature 462, 782–U101.

Cataldi, K., Shim, S.-H., Prakapenka, V.B., Zhao, J., Sturhahn, W., Chow, P., Xiao, Y., Liu, H., Cynn, H., Evans, W.J., 2010. Spin state of ferric iron in $MgSiO_3$ perovskite and its effect on elastic properties. Earth Planet. Sci. Lett. 289, 68–75.

Cataldi, K., Shim, S.-H., Dera, P., Prakapenka, V.B., Zhao, J., Sturhahn, W., Chow, P., Xiao, Y., Cynn, H., Evans, W.J., 2011. Effects of the Fe^{3+} spin transition on the properties of aluminous perovskite-new insights for lower-mantle seismic heterogeneities. Earth Planet. Sci. Lett. 310, 293–302.

Cottaar, S., Romanowicz, B., 2012. An unsually large ULVZ at the base of the mantle near Hawaii. Earth Planet. Sci. Lett. 355, 213–222.

Davies, G.F., 1974. Effective elastic-moduli under hydrostatic stress 1. Quasi-harmonic theory. Journal of Physics and Chemistry of Solids 35, 1513–1520.

Dorfman, S.M., Duffy, T.S., 2014. Effect of Fe-enrichment on seismic properties of perovskite and post-perovskite in the deep lower mantle. Geophys. J. Int. 197, 910–919.

Dudarev, S.L., Botton, G.A., Savrasov, S.Y., Humphreys, C.J., Sutton, A.P., 1998. Electron-energy-loss spectra and the structural stability of nickel oxide: an LSDA+U study. Phys. Rev. B 57, 1505–1509.

Flyvbjerg, H., Petersen, H.G., 1989. Error-estimates on averages of correlated data. J. Chem. Phys. 91, 461–466.

Fujino, K., Nishio-Hamane, D., Nagai, T., Seto, Y., Kuwayama, Y., Whitaker, M.L., Ohfuji, H., Shinmei, T., Irifune, T., 2014. Spin transition, substitution, and partitioning of iron in lower mantle minerals. Phys. Earth Planet. Inter. 228, 186–191.

Gialampouki, M., Xu, S., Morgan, D., 2018. Iron valence and partitioning between post-perovskite and ferropericlase in the Earth's lowermost mantle. Phys. Earth Planet. Inter. 282, 110–116.

Glazyrin, K., Ballaran, T.B., Frost, D.J., Mccammon, C., Kantor, A., Merlini, M., Hanfland, M., Dubrovinsky, L., 2014. Magnesium silicate perovskite and effect of iron oxidation state on its bulk sound velocity at the conditions of the lower mantle. Earth Planet. Sci. Lett. 393, 182–186.

Grocholski, B., Catalli, K., Shim, S.-H. & Prakapenka, V. 2012. Mineralogical effects on the detectability of the postperovskite boundary. Proceedings of the National Academy of Sciences of the United States of America, 109, 2275-2279.

Hernlund, J.W., Jellinek, A.M., 2010. Dynamics and structure of a stirred partially molten ultralow-velocity zone. Earth Planet. Sci. Lett. 296, 1–8.

Hernlund, J.W., Thomas, C., Tackley, P.J., 2005. A doubling of the post-perovskite phase boundary and structure of the Earth's lowermost mantle. Nature 434, 882–886.

Hess, S., Evans, D.J., 2001. Computation of the viscosity of a liquid from time averages of stress fluctuations. Phys. Rev. E 64, 112071–0112076.

Hsu, H., Umemoto, K., Blaha, P. & Wentzcovitch, R. M. 2010. Spin states and hyperfine interactions of iron in $(Mg,Fe)SiO_3$ perovskite under pressure. Earth Planet. Sci. Lett., 294, 19–26.

Hsu, H., Blaha, P., Cococcioni, M., Wentzcovitch, R.M., 2011. Spin-state crossover and hyperfine interactions of ferric iron in $MgSiO_3$ perovskite. Phys. Rev. Lett. 106, 1185011–1185014.

Ismailova, L., Bykova, E., Bykova, E., Cerantola, V., Mccammon, C., Boffa Ballaran, T., Bobrov, A., Sinmyo, R., Dubrovinskaia, N., Glazyrin, K., Liermann, H., Kupenko, I., Hanfland, M., Prescher, C., Prakapenka, V., Svitlyk, V. & Dubrovinsky, L. 2016. Stability of Fe,Al-bearing bridgmanite in the lower mantle and synthesis of pure Fe-bridgmanite. Sci. Adv., 2, e1600427.

Jensen, K., Thorne, M.S., Rost, S., 2013. SPdKS analysis of ultralow-velocity zones beneath the western Pacific. Geophys. Res. Lett. 40, 4574–4578.

Kresse, G., Furthmuller, J., 1996. Efficient iterative schemes for *ab-initio* total-energy calculations using a plane-wave basis set. Phys. Rev. B 54, 11169–11186.

Kresse, G., Joubert, D., 1999. From ultrasoft pseudopotentials to the projector augmented-wave method. Phys. Rev. B 59, 1758.

Kupenko, I., Mccammon, C., Sinmyo, R., Prescher, C., Chumakov, A. I., Kantor, A., Rueffer, R. & Dubrovinsky, L. 2014. Electronic spin state of Fe,Al-containing $MgSiO_3$ perovskite at lower mantle conditions. Lithos, 189, 167–172.

Kurnosov, A., Marquardt, H., Frost, D. J., Ballaran, T. B. & Ziberna, L. 2017. Evidence for a Fe^{3+}-rich pyrolitic lower mantle from (Al,Fe)-bearing bridgmanite elasticity data. Nature 543, 543.

Li, L., Brodholt, J.P., Stackhouse, S., Weidner, D.J., Alfredsson, M., Price, G.D., 2005. Elasticity of $(Mg, Fe)(Si, Al)O_3$ perovskite at high pressure. Earth Planet. Sci. Lett. 240, 529–536.

Liu, J., Dorfman, S.M., Zhu, F., Wang, Y., Zhang, D., Xiao, Y., Bi, W., Alp, E.E., 2018. Valence and spin states of iron are invisible in Earth's lower mantle. Nat. Commun. 9, 1284.

Mao, W. L., Shen, G. Y., Prakapenka, V. B., Meng, Y., Campbell, A. J., Heinz, D. L., Shu, J. F., Hemley, R. J. & Mao, H. K. 2004. Ferromagnesian postperovskite silicates in the D " layer of the earth. Proceedings of the National Academy of Sciences of the United States of America, 101, 15867-15869.

Mao, Z., Lin, J.F., Yang, J., Inoue, T., Prakapenka, V., 2015. Effects of the Fe^{3+} spin transition on the equation of state of bridgmanite. Geophys. Res. Lett. 42, 4335–4342.

Mcnamara, A.K., Garnero, E.J., Rost, S., 2010. Tracking deep mantle reservoirs with ultra-low velocity zones. Earth Planet. Sci. Lett. 299, 1–9.

Muir, J.M.R., Brodholt, J., 2015a. Elastic properties of ferropericlase at lower mantle conditions and its relevance to ULVZs. Earth Planet. Sci. Lett. 417, 40–48.

Muir, J.M.R., Brodholt, J., 2015b. Elastic properties of ferrous bearing $MgSiO_3$ and their relevance to ULVZs. Geophys. J. Int. 201, 496–504.

Muir, J.M.R., Brodholt, J.P., 2016. Ferrous iron partitioning in the lower mantle. Phys. Earth Planet. Inter. 257, 12–17.

Murakami, M., Hirose, K., Sata, N., Ohishi, Y., 2005. Post-perovskite phase transition and mineral chemistry in the pyrolitic lowermost mantle. Geophys. Res. Lett. 32.

Nishio-Hamane, D., Fujino, K., Seto, Y., Nagai, T., 2007. Effect of the incorporation of FeAlO3 into MgSiO3 perovskite on the post-perovskite transition. Geophys. Res. Lett. 34.

Nishio-Hamane, D., Seto, Y., Fujino, K., Nagai, T., 2008. Effect of FeAlO3 incorporation into MgSiO3 on the bulk modulus of perovskite. Phys. Earth Planet. Inter. 166, 219–225.

Nishiyama, N., Yagi, T., Ono, S., Gotou, H., Harada, T., Kikegawa, T., 2007. Effect of incorporation of iron and aluminum on the thermoelastic properties of magnesium silicate perovskite. Phys. Chem. Miner. 34, 131–143.

Nose, S., 1984. A molecular-dynamics method for simulations in the canonical ensemble. Mol. Phys. 52, 255–268.

Perdew, J.P., Burke, K., Ernzerhof, M., 1996. Generalized gradient approximation made simple. Phys. Rev. Lett. 77, 3865.

Perdew, J.P., Burke, K., Ernzerhof, M., 1997. Erratum: generalized gradient approximation made simple. Phys. Rev. Lett. 78, 1396.

Piet, H., Badro, J., Nabiei, F., Dennenwaldt, T., Shim, S., Cantoni, M., Hebert, C. & Gillet, P. 2016. Spin and valence dependence of iron partitioning in Earth's deep mantle. Proceedings of the National Academy of Sciences of the United States of America, 113, 11127-11120.

Saikia, A., Ballaran, T.B., Frost, D.J., 2009. The effect of Fe and Al substitution on the compressibility of MgSiO3-perovskite determined through single-crystal X-ray diffraction. Phys. Earth Planet. Inter. 173, 153–161.

Shukla, G., Wentzcovitch, R., 2016. Spin crossover in (Mg,Fe3+)(Si,Fe3+)O3 bridgmanite: effects of disorder, iron concentration, and temperature. Phys. Earth Planet. Inter. 260, 53–61.

Shukla, G., Wu, Z., Hsu, H., Floris, A., Cococcioni, M., Wentzcovitch, R., 2015a. Thermoelasticity of Fe^{2+}-bearing bridgmanite. Geophys. Res. Lett. 42, 1741–1749.

Shukla, G., Topsakal, M., Wentzcovitch, R., 2015b. Spin crossovers in iron-bearing $MgSiO_3$ and $MgGeO_3$: their influence on the post-perovskite transition. Phys. Earth Planet. Inter. 279, 11–17.

Shukla, G., Cococcioni, M., Wentzcovitch, R., 2016. Thermoelasticity of Fe^{3+}- and Al-bearing bridgmanite: effects of iron spin crossover. Geophys. Res. Lett. 43, 5661–5670.

Sinmyo, R., 2017. The spin state of Fe3+ in lower mantle bridgmanite. Am. Mineral. 102, 1263–1269.

Sun, N., Wei, W., Han, S., Song, J., Li, X., Duan, Y., Prakapenka, V. & Mao, Z., 2018. Phase transition and thermal equations of state of (Fe, Al)-bridgmanite and post-perovskite: implication for the chemical heterogeneity at the lowermost mantle. Earth Planet. Sci. Lett. 490, 161–169.

Tateno, S., Hirose, K., Sata, N., Ohishi, Y., 2005. Phase relations in Mg3Al2Si3O12 to 180 GPa: effect of Al on post-perovskite phase transition. Geophys. Res. Lett. 32.

Thorne, M.S., Garnero, E.J., Jahnke, G., Igel, H., Mcnamara, A.K., 2013. Mega ultra low velocity zone and mantle flow. Earth Planet. Sci. Lett. 364, 59–67.

Wang, X., Tsuchiya, T., Hase, A., 2015. Computational support for a pyrolitic lower mantle containing ferric iron. Nat. Geosci. 8, 556–560.

Wang, X.L., Tsuchiya, T., Zeng, Z., 2019. Effects of Fe and Al incorporations on the bridgmanite-postperovskite coexistence domain. Compt. Rendus Geosci. 351, 141–146.

Wentzcovitch, R., Justo, J. F., Wu, Z., Da Silva, C. R. S., Yuen, D. & Kohlstedt, D. 2009. Anomalous compressibility of ferropericlase throughout the iron spin cross-over. Proceedings of the National Academy of Sciences, 106, 8447-8452.

Wentzcovitch, R.M., Wu, Z.Q., Carrier, P., 2010. First principles quasiharmonic thermoelasticity of mantle minerals. In: Wentzcovitch, R., Stixrude, L. (Eds.), Theoretical and Computational Methods in Mineral Physics: Geophysical Applications. Chantilly, Mineralogical Soc Amer.

Wicks, J.K., Jackson, A., Sturhahn, W., 2010. Very low sound velocities in iron-rich (Mg,Fe)O: implications for the core-mantle boundary region. Geophys. Res. Lett. 37, L153041–L153045.

Wicks, J.K., Jackson, J.M., Sturhahn, W., Zhang, D.Z., 2017. Sound velocity and density of magnesiowustites: implications for ultralow-velocity zone topography. Geophys. Res. Lett. 44, 2148–2158.

Wu, Z., Wentzcovitch, R., 2014. Spin crossover in ferropericlase and velocity heterogeneities in the lower mantle. PNAS 111, 10468–104672.

Xu, S., Shim, S., Morgan, D., 2015. Origin of Fe^{3+} in Fe-containing, Al-free mantle silicate perovskite. Earth Planet. Sci. Lett. 409, 319–328.

Yu, Y.G., Hsu, H., Cococcioni, M., Wentzcovitch, R.M., 2012. Spin states and hyperfine interactions of iron incorporated in MgSiO3 post-perovskite. Earth Planet. Sci. Lett. 331, 1–7.

Zhang, S., Cottaar, S., Liu, T., Stackhouse, S., Militzer, B., 2016. High-pressure, temperature elasticity of Fe-and Al-bearing $MgSiO_3$: implications for the Earth's lower mantle. Earth Planet. Sci. Lett. 434, 264–273.

Zhao, C., Garnero, E., Li, M., Mcnamara, A.K., Yu, S., 2017. Intermittent and lateral varying ULVZ structure at the northeastern margin of the Pacific LLSVP. Journal of Geophysical Research Solid Earth 122, 1198–1220.